Spatial organization of lysosomal exocytosis relies on membrane tension gradients

Hugo Lachuer, Laurent Le, Sandrine Lévêque-Fort, Bruno Goud, Kristine Schauer

PNAS RESEARCH ARTICLE | CELL BIOLOGY
BIOPHYSICS AND COMPUTATIONAL BIOLOGY

Spatial organization of lysosomal exocytosis relies on membrane tension gradients

Hugo Lachuer[a], Laurent Le[b], Sandrine Lévêque-Fort[b], Bruno Goud[a], and Kristine Schauer[a,c,1]

Edited by Ana Maria Cuervo, Albert Einstein College of Medicine, Bronx, NY; received April 29, 2022; accepted December 17, 2022

Lysosomal exocytosis is involved in many key cellular processes but its spatiotemporal regulation is poorly known. Using total internal reflection fluorescence microscopy (TIRFM) and spatial statistics, we observed that lysosomal exocytosis is not random at the adhesive part of the plasma membrane of RPE1 cells but clustered at different scales. Although the rate of exocytosis is regulated by the actin cytoskeleton, neither interfering with actin or microtubule dynamics by drug treatments alters its spatial organization. Exocytosis events partially co-appear at focal adhesions (FAs) and their clustering is reduced upon removal of FAs. Changes in membrane tension following a hypo-osmotic shock or treatment with methyl-β-cyclodextrin were found to increase clustering. To investigate the link between FAs and membrane tension, cells were cultured on adhesive ring-shaped micropatterns, which allow to control the spatial organization of FAs. By using a combination of TIRFM and fluorescence lifetime imaging microscopy (FLIM), we revealed the existence of a radial gradient in membrane tension. By changing the diameter of micropatterned substrates, we further showed that this gradient as well as the extent of exocytosis clustering can be controlled. Together, our data indicate that the spatial clustering of lysosomal exocytosis relies on membrane tension patterning controlled by the spatial organization of FAs.

Vamp7 | exocytosis | Ripley's K function | membrane tension | focal adhesions

Significance

We show a role of membrane tension in lysosomal exocytosis. This process supports the release of molecules and vesicles from intracellular compartments called late endosomes/lysosomes. Lysosomal exocytosis is key to the repair and growth of the plasma membrane, the remodeling of the cell microenvironment and cell communication. It has also fundamental importance for virus release, cancer cell invasion, and lysosomal storage disorders. Thus, lysosomal exocytosis is a function of broad interest but not well understood. We reveal that a gradient of membrane tension in cells, organized by cellular adhesions, plays in important role in defining how lysosomal exocytosis is organized.

Exocytosis is an evolutionary novelty shared among all eukaryotes (i.e., a synapomorphy) (1). It relies on the SNARE machinery probably inherited from an archaeal ancestor (2). In addition to Golgi-derived vesicles along the secretory pathway, late endosomes, lysosomes and lysosome-related organelles also undergo exocytosis. Lysosomal exocytosis (referred to the secretion from late endosomes/lysosomes) is involved in the secretion of enzymes (3) and exosomes (4). It supports plasma membrane (PM) repair (5) as well as the remodeling of the microenvironment. Besides these general functions, lysosomal exocytosis fulfills specific roles in several cell types, such as the growth of neurites (6), axonal myelination (7), cell communication through ATP release in astrocytes (8), pseudopode formation in phagocytosis (9), secretion of cytotoxic granules in lymphocytes (10), MHC-II antigen presentation (11) and bone resorption in osteoclasts (12). It has a fundamental importance in several pathological contexts. For instance, lysosomal exocytosis is exploited by some β-coronavirus for their egress (13, 14) or by cancer cells to enhance invasion through the secretion of metalloproteases, especially at invadopodia (15, 16). Importantly, impairment of lysosomal exocytosis has been implicated in lysosomal storage disorders (LSDs) (17). Enhancing lysosomal exocytosis to release undigested lysosomal contents is a promising therapeutic strategy in these diseases (3).

Seminal work on the molecular machinery maintaining exocytosis, particularly vesicular (v-) and target (t-) SNAREs that are critical for the fusion of secretory vesicles arriving at the PM (18–20), uncovered key mechanisms that regulate the frequency of secretory events (21, 22). Exocytosis has been known to be polarized toward active zones in neuronal cells for a long time (23). In recent years, the question has arisen where exocytosis takes place and how cells regulate secretion at specific cellular sites in non-neuronal cells. After some conflicting results (24, 25), it has been now clearly demonstrated that exocytosis is not random but clustered even in nonpolarized cells (26–29). The evidence also exists that lysosomal intracellular positioning is non-random (30, 31). Moreover, in polarized epithelial cells, lysosomal exocytosis is targeted to the basolateral membrane (32). However, the spatial regulation of exocytosis in nonpolarized cells and its mechanisms have not been explored.

Lysosomal exocytosis relies on VAMP7 (33–35), a v-SNARE that is insensitive to tetanus and botulinum neurotoxins (hence its other names TI-VAMP for Tetanus neurotoxin Insensitive Vesicle-Associated Membrane Protein) (36). In epithelial cells, VAMP7 interacts with the t-SNAREs syntaxin (STX) 3 (37) and STX4 (38) found at the PM and with STX7. Whereas STX3/4 are involved in exocytosis, STX7 is only involved in intracellular endosomal fusion events (39–41).

Author contributions: H.L. and K.S. designed research; H.L. performed research; H.L., L.L., and S.L.-F. contributed new reagents/analytic tools; H.L., L.L., and S.L.-F. analyzed data; and H.L., B.G., and K.S. wrote the paper.

The authors declare no competing interest.

This article is a PNAS Direct Submission.

[1]To whom correspondence may be addressed. Email: kristine.schauer@gustaveroussy.fr.

This article contains supporting information online at https://www.pnas.org/lookup/suppl/doi:10.1073/pnas.2207425120/-/DCSupplemental.

Published February 17, 2023.

In the present study, we use tools from spatial statistics to analyze live imaging data of fluorescent VAMP7 obtained by TIRFM on RPE1 cells undergoing lysosomal exocytosis. RPE1 cells phagocyte retinal photoreceptors (cones and rods) outer segments to support photoreceptor renewal and have been shown to conserve a high phagocytosis rate in cultured cell condition that is balanced by a high exocytosis (42, 43). We report that spatial organization of lysosomal exocytosis relies on a membrane tension gradient and the spatial distribution of FAs.

Results

1) Exocytosis from Lysosomes Is not Random. To monitor lysosomal exocytosis, we transfected RPE1 cells with a pHluorin construct of the v-SNARE VAMP7, VAMP7-pHluorin. The pHluorin signal is quenched in the lumen of acidic vesicles but unquenched during exocytosis when protons from the lysosomal lumen are released (Fig. 1*A*). Using dynamic TIRFM imaging, we manually detected exocytosis events characterized by a sudden increase in intensity followed by a decay clearly visualized in kymographs (Fig. 1*B* and Movie S1). The decrease in intensity corresponds to the 2D diffusion of VAMP7-pHluorin in the plane of the PM. Its diffusion kinetic can be fitted by a single decreasing exponential function with a half-life of about 1.69 ± 0.83 s (*SI Appendix*, Fig. S1 *A* and *B*). The detected exocytosis can be represented by an intensity map where the intensity λ represents the local expected number of event/μm^2 (Fig. 1*C*). VAMP7 has been reported as a marker of endosomal/lysosomal compartments but overexpression could create an artificial accumulation in recycling endosomes. Colocalization experiments in fixed cells demonstrate that the overexpressed VAMP7-pHluorin does not colocalize with endosomes marked by Rab11 antibody (Fig. 1*D*) but with lysosomes marked with LAMP1 antibody (Fig. 1*E*) and LysoTracker (Fig. 1*F*). Note that cells loaded with Lysotracker are subsequently fixed and therefore lysosomes are no longer acidic, impairing pHluorin quenching. The colocalization is quantified using Manders coefficient, i.e., the fraction of segmented VAMP7 structures included in segmented organelles (endosomes and lysosomes) (Fig. 1*G*). It confirms that VAMP7 overexpression does not induce any mistargeting. RPE1 cells display a high lysosomal exocytosis rate as several hundred exocytosis events in a typical cell could be observed within 5 min, corresponding to an exocytosis rate of $39 \times 10^{-5} \pm 31 \times 10^{-5}$ exocytosis/μm^2/s (Fig. 1*H*). Because VAMP7 substantially colocalizes with Golgi-derived vesicles in some cell types (44), especially in neuronal cells (45), we further tested that monitored exocytosis events are bonafide lysosomal exocytosis events. To confirm that VAMP7 specifically marks lysosomal exocytosis in RPE1 cells, we treated cells with Golgicide A, an inhibitor of the Arf1 GEF (Guanine nucleotide Exchange Factor) GBF1, which induces Golgi apparatus dispersion and inhibits the Golgi-derived vesicles secretion (46). As shown in (Fig. 1*I* and Movie S2), Golgicide A did not significantly alter the exocytosis rate. Contrary, inhibition of the lysosomal V-type ATPase using Bafilomycin A1 significantly reduced the exocytosis rate (Fig. 1*J* and Movie S3). Lysosomal exocytosis can be stimulated by histamine through the G1q-PKC pathway (47). As expected, treating RPE1 cells with histamine significantly increased the exocytosis rate (Fig. 1*K* and Movie S4) immediately after the addition of histamine (*SI Appendix*, Fig. S1*C*). Taken together, these results demonstrate that VAMP7 exocytosis represents bonafide lysosomal exocytosis in RPE1 cells.

The obtained exocytosis maps can be visualized as patterns of points (Fig. 1*C*). Such patterns can be the result of an uniformly random process (Complete Spatial Randomness, CSR) or reflects either clustering (i.e., aggregation) or dispersion (i.e., ordering with an inhibition surface around each point of exocytotic event) (48, 49). We obtained a large dataset of 183 cells showing 32.880 exocytosis events to test the CSR hypothesis and to characterize the spatiotemporal properties of lysosomal exocytosis. The observed spatiotemporal characteristics of exocytosis were compared to CSR Monte Carlo simulations (*Methods*). First, we found that exocytosis events present a smaller nearest-neighbor distance (NND) than expected in the case of CSR, which indicates clustering at the scale of immediate neighbors (Fig. 1*L*). Moreover, events are more distant to cell borders than expected demonstrating that exocytosis is much less frequent close to cell borders (Fig. 1*M*). Events are also anisotropically distributed in the cells, i.e., have a preferential direction (Fig. 1*N*). To explore this anisotropy, we seeded cells on rectangular micropatterns forcing the orientation of cells into two possible directions (left or right) (*SI Appendix*, Fig. S1*D* and Movie S5). Results confirmed anisotropy in exocytosis and showed that the secretory direction correlates with the Golgi-Nucleus axis (*SI Appendix*, Fig. S1*D*).

The most pertinent tool to analyze a spatial structure is the Ripley's K function that measures the average number of neighbor events at a given scale. The average curve obtained from observed events significantly deviated from the expected one in case of CSR, indicating clustering of lysosomal exocytosis, even at the scale of several micrometers (Fig. 1*O*). The CSR envelope is not symmetric around 0, reflecting a slight bias introduced by the boundary corrections in the computation of the Ripley's K function. Note that the treatment with Golgicide A, Bafilomycin A1, and histamine did not change the spatial organization of exocytosis (*SI Appendix*, Fig. S1 *E–G*), indicating that the rate and spatial patterning of exocytosis are independent features. We noticed a slight correlation between exocytosis rate and clustering (*SI Appendix*, Fig. S1*H*). This correlation is not due to a bias in the measure, because Ripley's K function is independent on the number of events (50) and indeed, conserving an arbitrary percentage of the recorded events does not affect the Ripley's K function (*SI Appendix*, Fig. S1*I*). We conducted a similar analysis for the temporal distribution of exocytosis events. The temporal Ripley's K function demonstrates a temporal clustering (*SI Appendix*, Fig. S1*J*). However, a Fourier analysis revealed that this clustering is not due to a periodicity in the exocytosis rate (*SI Appendix*, Fig. S1*K*). Lastly, we quantified the coupling between spatial and temporal dimensions using the spatiotemporal Ripley's K function (*SI Appendix*, Fig. S1*L*), which provides information about the independency of the temporal and spatial coordinates. This analysis revealed that a substantial proportion of cells presents a spatiotemporal coupling and among cells with a significant coupling, 82.7% have a positive coupling i.e., events that are close in space are also more likely to be close in time. Together, our analysis confirmed that lysosomal exocytosis is a non-random process in space and time.

2) Lysosomal Exocytosis Is coupled to Central Focal Adhesions in a Cytoskeleton-Independent Manner. To investigate the mechanisms underlying the spatial clustering of lysosomal exocytosis events, we first tested whether the t-SNAREs interacting with VAMP7 show clustering, as proposed previously (32). Therefore, we analyzed the spatial patterns of STX3 and STX4 (*SI Appendix*, Fig. S2 *A–C*). Although STX3/4 presented a significant clustering, it was much weaker than the one of exocytosis events. Thus, we next focused on FAs, shown to be targeted by a subpopulation of lysosomes that were characterized to be positive for the MAPK scaffold complex p14-MP1 (p14-MP1+) (51) as well as by Golgi-derived

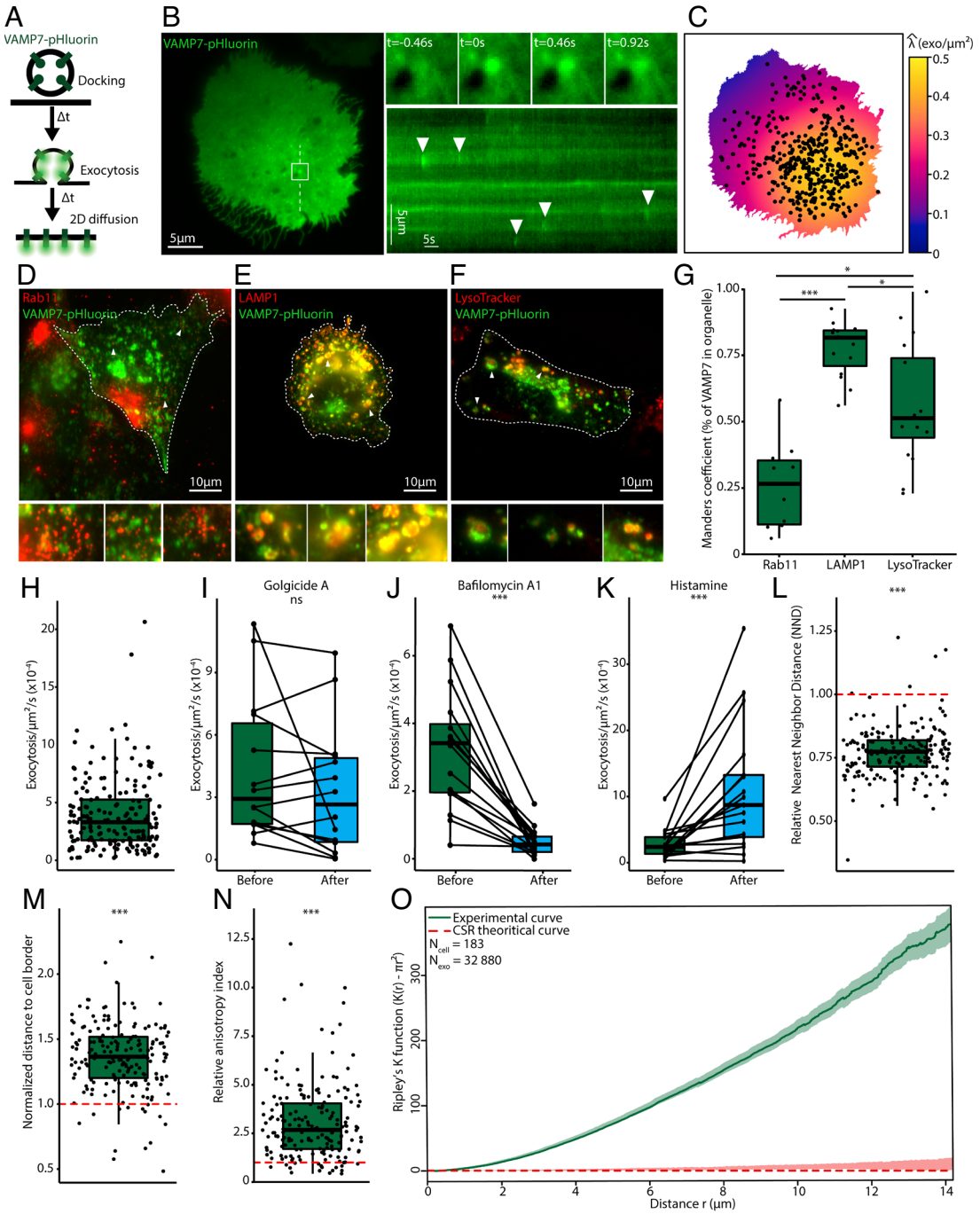

Fig. 1. Lysosomal Exocytosis Is Not Random but Clustered. (*A*) Schematic representation of the exocytosis of a VAMP7-pHluorin+ vesicle: the low pH of the acidic lumen quenches the fluorescence of pHluorin. During exocytosis, protons are released and pHluorin starts to emit light. An exocytosis event is followed by the 2D diffusion of VAMP7-pHluorin at the PM. (*B*) TIRFM image of VAMP7-pHluorin in a transfected RPE1 cell. The inset represents the field in the white square showing one exocytosis event at different time points, t = 0 represents the beginning of the exocytosis event. A kymograph is plotted along the dashed white line and arrowheads indicate several observed exocytosis events. (*C*) Exocytosis intensity map of the cell in *B* acquired during 5 min. Black dots represent exocytosis events. The color code represents the estimation of the local intensity $\hat{\lambda}$ expressed in exocytosis/µm^2. (*D–F*) Colocalization between Rab11, LAMP1 and LysoTracker with over-expressed VAMP7-pHluorin. Insights indicated by arrowheads emphasize on colocalization details. Insights of Rab11 staining have a different contrast to highlight small vesicles not visible in the full size image. Insights of LysoTracker signal reveal that LysoTracker signal accurately stains lysosomal lumen whereas VAMP7 signal is membranous. (*G*) Colocalization quantified with Manders coefficient (i.e., fraction of VAMP7 segmented structures overlapping with Rab11/LAMP1/Lysotracker segmented structures). The significance has been evaluated using Kruskal-Wallis test and a post hoc Dunn's test, $*P < 0.05$ and $***P < 0.001$, 10 cells were analyzed for Rab11 staining, 14 cells for LAMP1 staining and 15 cells for LysoTracker staining. (*H*) Normalized exocytosis rate in RPE1 cells from n = 183 cells (and 32,880 exocytosis events) from 34 independent experiments; ($3.9 \times 10^{-4} \pm 3.1 \times 10^{-4}$ exocytosis/s/µm^2). (*I*) Exocytosis rate before and after Golgicide A (10 µM, 30 min) treatment; n = 14 cells from three independent experiments. (*J*) Exocytosis rate before and after bafilomycin A1 (100 nM, 60 min) treatment; n = 16 cells from three independent experiments. (*K*) Exocytosis rate before apara-nitroblebbistatinnd after histamine (100 µM, cells immediately imaged) treatment; n = 17 cells from three independent experiments. In *I–K*, significance has been evaluated with paired Wilcoxon test, ns $P > 0.05$ and $***P < 0.001$. (*L*) Relative Nearest Neighbor Distance ($NND_{observed}/NND_{simulated}$) of basal exocytosis observed in *H*. (*M*) Relative distance to cell borders ($distance_{observed}/distance_{simulated}$) of basal exocytosis observed in *H*. (*N*) Relative anisotropy index ($anisotropy_{observed}/anistropy_{simulated}$) of basal exocytosis observed in *H*. 90% of the cells have a relative anisotropy index superior to 1. In (*L–N*), the red dotted line represents expected value under CSR hypothesis and the significance of the deviation to CSR has been computed using a *t* test. $***P < 0.001$. (O). Average centered Ripley's K function [$K(r)-\pi r^2$] of 183 cells (and 32.880 exocytosis events) observed in *H*. Green curve represents the experimental results ± SEM and the red dotted line the expectation under CSR hypothesis. Red shade represents envelope containing 95% of CSR simulations.

Rab6+ vesicles (52). We quantified the co-appearance of VAMP7-pHluorin with FAs using the FA protein paxillin (Paxillin-mCh) as a marker in co-transfected cells (Fig. 2 *A* and *B* and Movie S6). The co-appearance index was significantly higher than expected from CSR Monte Carlo simulations (Fig. 2*B*). Interestingly, VAMP7 lysosomal exocytosis mainly appeared at central FAs, defined by a distance superior to 3 μm from cell borders (*SI Appendix,* Fig. S2*D*), consistent with the observation that exocytosis frequency is low close to cell borders (Fig. 2*A*). Exocytosis events were found both at central FAs and at their close periphery. To further test the role of FAs, we cultured cells on poly-L-lysine (PLL) substrates to inhibit the formation of FAs (*SI Appendix*, Fig. S2*E* and Movie S7). Under this condition, the clustering of lysosomal exocytosis decreased significantly (Fig. 2*C*), indicating a role of FAs in the spatial organization of exocytosis. We noticed that exocytosis rate was significantly enhanced on PLL substrate, probably due to a smaller adhesive surface under this condition (*SI Appendix*, Fig. S2*F*). To investigate whether the enrichment of exocytosis events at FAs is biochemically mediated (i.e., signaling) or mechanically mediated, we inhibited the focal adhesion kinase (FAK). FAK is a major FA signaling hub, especially involved in integrin-mediated signal transductions (53). We inhibited FAK with PF-573228 (at 10 μM for 15 min), a molecule described as preserving FAs topography by inhibiting their turn over (54). FAK inhibition did not change spatial structure of lysosomal exocytosis events suggesting a mechanical regulation (*SI Appendix*, Fig. S2*G* and Movie S8). Noteworthy, the FAK inhibition causes a decrease of exocytosis rate (*SI Appendix,* Fig. S2*H*) demonstrating that spatial structure and exocytosis rate are two independent parameters.

FAs are closely linked to both microtubules (MT) (+) ends (55–57), and the cortical acto-myosin cytoskeleton (58). Surprisingly, MT depolymerization by nocodazole treatment did not reduce clustering (Fig. 2*D* and Movie S9) nor the exocytosis rate (Fig. 2*E*). The depolymerization of F-actin by a low dose of cytochalasin D significantly reduced the exocytosis rate (Fig. 2*G* and Movie S10), however, did not reduce lysosomal clustering (Fig. 2*F*) confirming that these parameters are independent. This suggested a role of actin in facilitating fusion of lysosomes with PM but not in the organization of exocytosis patterning. Moreover, myosin-2 (MYH9) inhibition by para-nitroblebbistatin treatment affected neither exocytosis clustering nor exocytosis rate (Fig. 2 *H* and *I* and Movie S1). These treatments can cause cell retraction but we controlled that these treatments do not alter the FA density per cell (*SI Appendix Fig.* S2 *I* and *J*). Taken together, these results demonstrate that FAs can regulate lysosomal exocytosis patterns in a cytoskeleton-independent manner. Moreover, they confirm a targeting of lysosomal secretion events to central FAs and exclusion from external one**s.**

3) Exocytosis Clustering Relies on Membrane Tension. We tested the role of physical parameters, such as membrane tension, known to regulate the exocytosis rate (59–64). We applied a hypo-osmotic shock and monitored VAMP7 exocytosis 15 min after the shock. Hypo-osmotic shock causes cell swelling leading to an immediate increased membrane tension followed by a slow recovery (65). VAMP7+ exocytosis has been reported to be less frequent after hyper-osmotic shock (64) and hypo-osmotic shock increased exocytosis rate in experimental and theoretical models (66, 67). Surprisingly, the hypo-osmotic shock significantly reduced the exocytosis rate in RPE1 cells (Fig. 3*B* and Movie S12). However, hypo-osmotic shock significantly increased the clustering of lysosomal exocytosis (Fig. 3*A*). It also increased the co-appearance between exocytosis events and FAs (Fig. 3*C* and Movie S13). To further confirm these results, we treated cells with methyl-β-cyclodextrin that depletes cholesterol from the PM and was shown to increase membrane tension (68–70). Cyclodextrin treatment significantly increases clustering, similarly to hypo-osmotic shock treatment (Fig. 3*D*). Moreover, cyclodextrin treatment also decreases exocytosis rate (Fig. 3*E* and Movie S14) and increases the co-appearance between exocytosis events and FAs (Fig. 3*F* and Movie S15). These treatments can cause cell retraction, but we controlled that these treatments do not alter the FA density per cell (*SI Appendix*, Fig. S3 *A* and *B*).

Next, we directly measured membrane tension using the Fluorescence Lifetime Imaging Microscopy (FLIM) probe Flipper-TR (71). The Flipper-TR intercalates in membranes, where the membrane microenvironment favors one of two possible molecular conformations of the Flipper-TR (planar or orthogonal). The two conformations display different fluorescence lifetimes. Higher local membrane tension leads to higher fluorescence lifetimes (Fig. 3*H*). We quantified fluorescence lifetime in living cells using a TIRF-FLIM device under different experimental conditions. We observed that the membrane tension at the ventral part of the cell is not homogeneous in cells seeded on fibronectin-coated surface. Interestingly, we found that membrane tension presents variability compatible with the micrometer scale of exocytosis clustering (Fig. 3*G*). Surprisingly, no significant variation in the Flipper-TR fluorescence lifetime was observed following a hypo-osmotic shock (*SI Appendix*, Fig. S3 *C* and *D*), performed with the same delay than experiments in Fig. 3*A*. This lack of variation could probably be due to a recovery of membrane tension that could have occurred in the 15-min incubation period between applying a hypo-osmotic shock and the measurement. We found that methyl-β-cyclodextrin significantly reduced Flipper-TR fluorescence lifetime, indicative of a decrease of membrane tension (*SI Appendix*, Fig. S3 *B–D*) congruently with a previous study (72). However, the effect could be due to a change in membrane order, also known to affect Flipper-TR (71). This result suggests that the total average membrane tension does not regulate exocytosis pattern. Because lysosomal clustering is regulated by FAs, we next quantified fluorescence lifetime in living cells seeded on PLL-coated surface. Despite their difference in exocytosis clustering, the average lifetime was again similar in these two conditions (Fig. 3*I*). Together, these results indicate that global membrane tension does not regulate clustering of exocytosis. However, cells grown on fibronectin showed clustering of similar lifetime values at several regions, whereas these values appeared more homogeneously distributed in cells on PLL (Fig. 3*G*). Thus, we measured the spatial auto-correlation using the Moran's index, which increases in case of clustering of pixels values. Moran's index was indeed significantly higher in cells plated on fibronectin than on PLL (Fig. 3*J*). This suggests that the spatial organization of lysosomal exocytosis could be controlled by regional heterogeneity in membrane tension rather than the global tension at the whole cell level. Moreover, our results indicate that the presence of FAs favors a compartmentalization of membrane tension.

4) Intracellular Coupling Between Exocytosis Probability and Membrane Tension. A simultaneous observation of the Flipper-TR signal and exocytosis events is technically very challenging. Therefore, to correlate membrane tension and exocytosis events, we normalized RPE1 cell geometries using adhesive ring-shaped micropatterns. An advantage of micropatterned cells is the possibility to standardize the adhesive surface and FA distribution. On ring-shaped micropatterns (Fig. 4*A*), FAs are formed at the inner and outer borders of the ring mimicking the inner and peripheral FAs found in non-patterned cells (*SI Appendix,* Fig. S4 *A* and *B*). Using the Ripley's K function, we found that

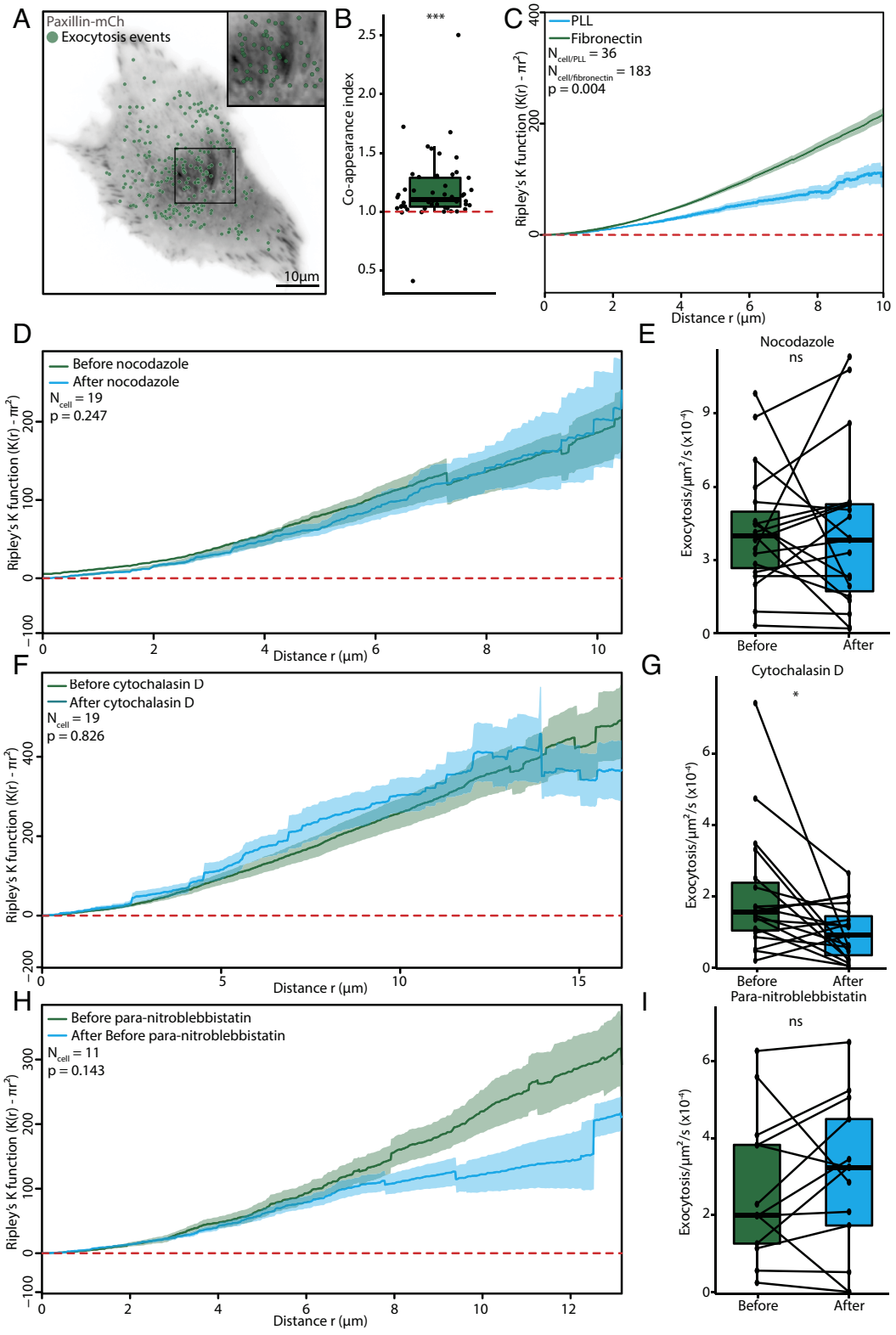

Fig. 2. Lysosomal Exocytosis Is Coupled to Central Focal Adhesions in a Cytoskeleton-Independent Manner. (*A*) Merge from TIRFM live cell imaging of a paxillin-mCh/VAMP7-pHluorin co-transfected RPE1 cell: the gray scale image represents snapshot of paxillin-mCh intensity and green dots represent exocytosis events localization. Insight emphasizes the proximity between exocytosis events and central FAs. (*B*) Co-appearance index between exocytosis events and FAs. Red dashed line represents expected co-appearance in the case of CSR. The significance of the deviation to CSR has been computed using a *t* test, ***$P < 0.001$; n = 49 cells from four independent experiments. (*C*) Average spatial Ripley's K function ± SEM for cells seeded on fibronectin (green curve) and PLL (blue curve); 36 cells on PLL and 183 cells on fibronectin were analyzed from 3 and 34 independent experiments, respectively. (*D*) Average spatial Ripley's K function ± SEM before (green) and after (blue) incubation with nocodazole (10 µM, 60 min). (*E*) Exocytosis rate before and after nocodazole treatment (10 µM, 60 min). (*D–E*): n = 19 cells analyzed from four independent experiments. (*F*) Average spatial Ripley's K function ± SEM before (green) and after (blue) cytochalasin D treatment (500 nM, 60 min). (*G*) Exocytosis rate before and after incubation with cytochalasin D (500 nM, 60 min). (*F–G*) 19 cells analyzed from three independent experiments. (*H*) Average spatial Ripley's K function ± SEM before (green) and after (blue) para-nitroblebbistatin treatment (20 µM, 15 min). (*I*) Exocytosis rate before and after para-nitroblebbistatin treatment (20 µM, 15 min). (*H* and *I*): n = 13 cells from three independent experiments were analyzed. In (*C*, *D*, *F* and *H*) the significance of the difference between Ripley's K functions has been evaluated using a permutation test (*Methods*) and red-dashed line represents expectation in the case of CSR. In *E*, *G* and *I*, the significance has been evaluated using a paired Wilcoxon test, ns $P > 0.05$, *$P < 0.05$.

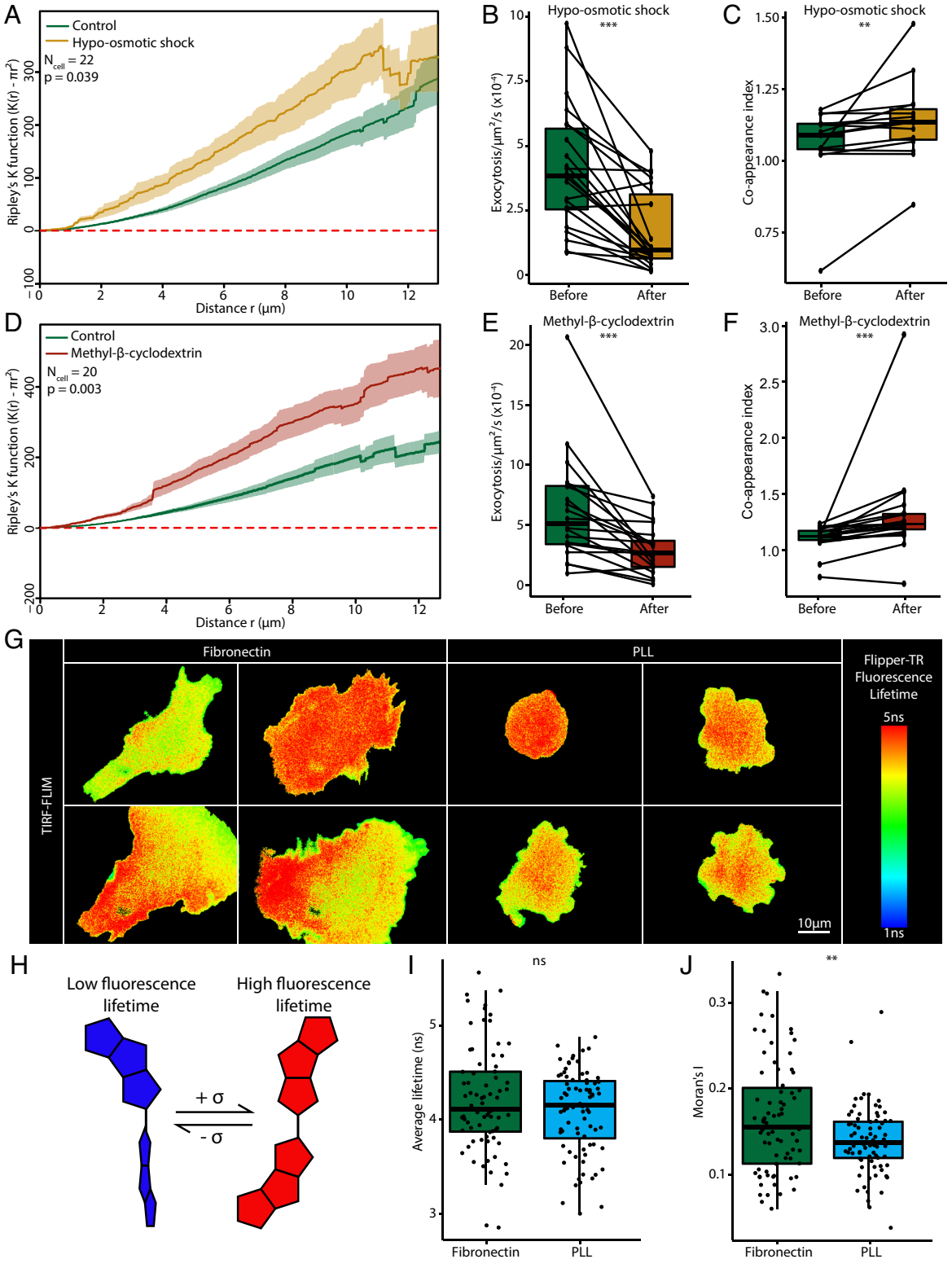

Fig. 3. Membrane tension regulates lysosomal exocytosis clustering. (*A*) Average spatial Ripley's K function ± SEM before (green) and after (yellow) hypo-osmotic shock (1:1 dilution, 15 min). (*B*) Exocytosis rate before and after hypo-osmotic shock. In *A* and *B*, 22 cells from four independent experiments were analyzed. (*C*) Co-appearance index between exocytosis spots and FAs before and after hypo-osmotic shock. 15 cells analyzed in three independent experiments. (*D*) Average spatial Ripley's K function ± SEM before (green) and after (dark-red) β-methyl-cyclodextrin addition (5 mM, 15 min). (*E*) Exocytosis rate before and after β-methyl-cyclodextrin addition. In *D* and *E*, 20 cells from three independent experiments were analyzed. (*F*) Co-appearance index between exocytosis spots and FAs before and after β-methyl-cyclodextrin; 19 cells from three independent experiments were analyzed. In *A* and *D*, the significance of the difference between Ripley's K functions has been evaluated using a permutation test (*Method*) and red-dashed line represents expected curve in the case of CSR. In *B*, *C*, *E*, and *F*, significance has been evaluated using paired Wilcoxon test, $^{**}P < 0.01$ and $^{**}P < 0.001$. (*G*) TIRF-FLIM images of each four representative cells seeded on either fibronectin or PLL substrate, and incubated with Flipper-TR. The color code represents the Flipper-TR fluorescence lifetime. (*H*) Schematic representation of the principle for membrane tension measurements by FLIM probe Flipper-TR. Under high membrane tension, the planar conformation is favored increasing its fluorescence lifetime, whereas low membrane tension favores the orthogonal conformation with low fluorescence lifetime. (*I*) Average fluorescence lifetime per cell seeded on fibronectin and PLL substrate. (*J*) Moran's I index per cell seeded on fibronectin and PLL substrate. In *I* and *J*, significance has been evaluated using *t* test, ns $P > 0.05$ and $^{**}P < 0.01$, 75 cells have been analyzed on fibronectin-coated surface, and 80 cells in PLL-coated, from three independent experiments.

the clustering of lysosomal exocytosis also occurs in patterned cells, although significantly weaker than in non-patterned cells (Fig. 4*B* and Movie S16). Plotting the radial average density of exocytosis events demonstrated that cells exhibit an enrichment of events at half of the cell radius as the density deviated there from the expected CSR case (Fig. 4*C*). This corresponds to a radius close to the internal FAs populations. Moreover, exocytosis events are less frequent at cell borders similarly to non-patterned cells. Using the same micropatterns, we then measured membrane tension by TIRF-FLIM. Interestingly, cells displayed a radial gradient of membrane tension with the lowest membrane tension values at the extreme cell border and in the center, and a linear increase in membrane tension for the center to the periphery (Fig. 4 *D* and *E*). The Moran's index is lower in patterned cells than in non-patterned cells despite the presence of the gradient (*SI Appendix*, Fig. S4*C*). Taken together with the PLL experiments, this result points out a correlation between clustering/compartmentalization of membrane tension and clustering of exocytosis. The cross-correlation between the normalized lifetime and the exocytosis probability demonstrates that the exocytosis probability increases with the membrane tension in a monotonous however non-linear manner (Fig. 4*F*). Note that the exocytosis probability is defined as the probability of exocytosis at a given place knowing that an event will occur. Therefore, it does not reflect the exocytosis rate but only its spatial distribution. The above results together indicate that exocytosis is favored at regions with high local membrane tension, and that these regions are spatially organized leading to clustering in these regions.

5) Strength of Membrane Tension Gradient Correlates with Clustering of Lysosomal Exocytosis. To further investigate the role of membrane tension in the spatial regulation of exocytosis, we established exocytosis and membrane tension maps of cells cultured on ring-shaped micropatterns of different sizes (Fig. 5*A* and Movie S17). The average membrane tension was found to be similar on all pattern sizes (*SI Appendix,* Fig. S5*A*). However, the membrane tension gradient varied according to the pattern size (Fig. 5*B*), except for cells plated on small patterns that did not display any gradient. Consistently, the Moran's index increased from small to large micropatterns (*SI Appendix,* Fig. S5*B*). Interestingly, the absence of a gradient in the smallest size micropatterns correlates with a lower level of clustering of exocytosis events, whereas the presence of a gradient in the largest cell size correlates with higher clustering (Fig. 5*C*). Noteworthy, here we only highlight spatial organization at a scale >2 μm since Ripley's K functions cannot be discriminated at a shorter scale. Therefore organization at smaller scales could be different as suggested by exocytosis map of small micropattern (Fig. 5*A*). On the other hand, the exocytosis rate (normalized to cell surface) was not significantly different regardless of the pattern sizes (*SI Appendix,* Fig. S5*C*). These results strongly suggest a role of the membrane tension gradient in the regulation of spatial exocytosis patterns.

Discussion

Our data demonstrate that lysosomal exocytosis is not random (i.e., CSR) but clustered in space and time with a positive coupling between spatial and temporal dimensions (Fig. 1). Lysosomal exocytosis occurs close to central FAs and it is almost absent at cell borders. In agreement with this result, cells seeded on PLL, which inhibits the formation of FAs, display a decreased clustering of exocytic events (Fig. 2). Previous work described a targeting of lysosomes to FAs but exocytosis at these points was not demonstrated (51). Our data suggest that clustering does not rely on an intact cytoskeleton as the spatial pattern of lysosomal exocytosis was not perturbed upon treatment with drugs affecting the cytoskeleton (Fig. 2). The underlying mechanism supporting clustering of exocytotic events from lysosomes at FA is likely different from the exocytosis of Golgi-derived vesicles. Indeed, clustering of Golgi-derived vesicles was shown to be inhibited by both actin and microtubule depolymerization (27). However, interfering with the actin cytoskeleton inhibits VAMP7-mediated exocytosis rate in neuronal cells (73) similarly to our observation (Fig. 2*G*). The involvement of the cytoskeleton in clustering of lysosomal and Golgi-derived exocytosis will then require further investigation in different cell types.

We found that interfering with membrane tension by hypo-osmotic shock and methyl-β-cyclodextrin treatments impact clustering of exocytosis, revealing a role of membrane tension in the spatial organization of exocytosis (Fig. 3). Our results complement previous data illustrating the role of membrane tension on the exocytosis rate (60–64, 74).

A previous study reported that in addition to changing total membrane tension, methyl-β-cyclodextrin treatment increases its heterogeneity (69). In addition, transmembrane proteins at FAs have been proposed to behave as obstacles to the lipid flow that equilibrates membrane tension (74). Cells seeded on PLL reveal a more uniform membrane tension, confirming the role of FAs as obstacles. Together, our data suggest that an inhomogeneity of membrane tension induced by FAs favors the accumulation of secretory events at these regions. This hypothesis is supported by experiments performed on micropatterns, which show that the symmetric arrangement of FAs is associated with a well-defined gradient of membrane tension (Fig. 4). Moreover, an increase in the micropattern diameter correlates with the strength of membrane tension gradient and exocytosis clustering (Fig. 5). Thus, other mechanisms or proteins that could regulate the heterogeneity of PM tension could potentially spatially regulate exocytosis. Interestingly, a gradient in membrane tension has been already observed in moving keratinocytes (75). Such a gradient could result from the friction between PM and either actin treadmilling or the adhesion substrate (76). In our experiments performed on non-migratory cells constrained by adhesion on micropatterns, only actin retrograde flow could potentially cause friction. Yet, experiments in non-patterned cells revealed that clustering is independent of the actin cytoskeleton. Thus, the above result could indicate that the diffusion of membrane tension in the PM is very slow, resulting in a stable gradient at the timescale of our experiments, similarly to what was previously observed in non-neuronal cells (62). Therefore, exocytosis organization could appear to be independent from cytoskeleton at time scales that are below those required for membrane tension to equilibrate that have been proposed to be in the timescale of several hours (62). Finally, the experiments on micropatterns revealed a positive coupling between exocytosis probability and membrane tension (Fig. 4). Of note, the absence of gradient in membrane tension observed in cells grown on small micropatterns does not totally abolish exocytosis clustering. This suggests that other mechanisms regulate clustering, such as for instance clustering of syntaxins. Indeed, our analysis does not provide sufficient resolution at low scales, including cholesterol-enriched or tetraspanins-enriched microdomains. Because these microdomains are known to be enriched with SNAREs to facilitate exocytosis, the observed decrease of exocytosis rate under different conditions indicates that mechanisms at the microscale should be further investigated. Moreover, the fact that Flipper-TR reports changes in membrane tension but also in lipid order (71) could complicate the interpretation of the cholesterol depletion by cyclodextrin treatment. In conclusion, we propose that the spatial clustering of lysosomal exocytosis relies

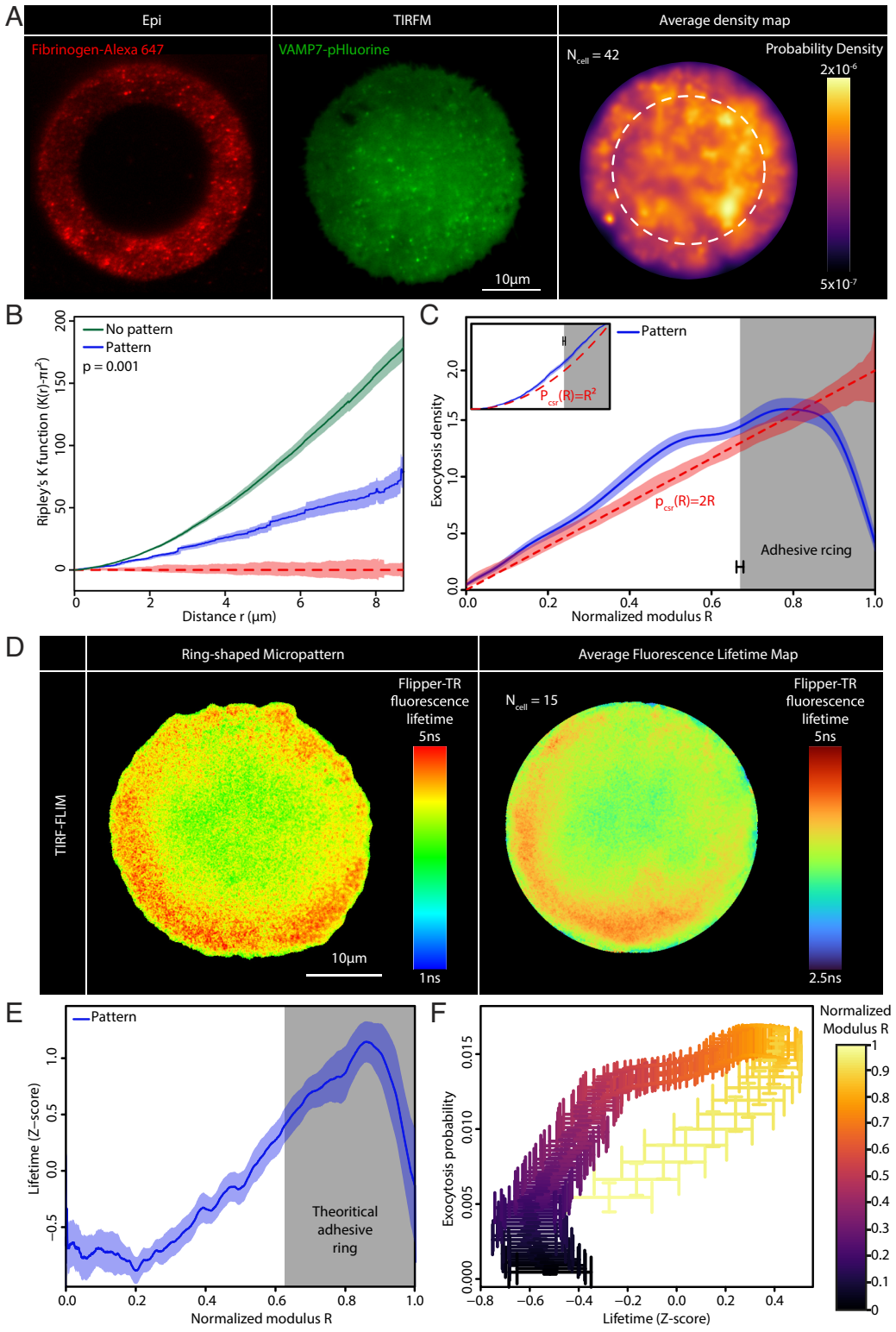

Fig. 4. Coupling Between Membrane Tension Gradients and Exocytosis Probability. (*A*) Representative epifluorescence image of a 37-µm-diameter ring-shaped micropattern stained with fibrinogene-Alexa647 and a TIRFM image of VAMP7-pHluorin transfected cell cultured on it accompanied by the average exocytosis map from 42 cells. The color code represents the probability to observe exocytosis knowing that one event occurred. (*B*) Average spatial Ripley's K function ± SEM of exocytosis in cells seeded on ring-shaped micropattern (blue) and non-patterned cells (green, same data as in F1H). The significance of the difference between Ripley's K functions has been evaluated using a permutation test (*Method*). (*C*) Average radial density ± SEM of exocytosis in cells seeded on ring-shaped micropattern. The modulus (distance to pattern center) is normalized to the cell radius, setting cell border at R = 1. The gray rectangle represents the average position of the adhesive part of the micropattern ± SEM. The inset represents the same data but as a cumulative density function instead of probability density. (*A*–*C*): 42 cells were analyzed from nine independent experiments. In *B* and *C*, the red-dashed line represents expected curve in the case of CSR and red shade represents envelope containing 95% of CSR simulations. (*D*) TIRF-FLIM image of a representative cell seeded on a ring-shaped micropattern and incubated with Flipper-TR, and average fluorescence lifetime map from TIRF-FLIM images of 15 cells. The color code represents Flipper-TR fluorescence lifetime. (*E*) Radial average ± SEM of the Flipper-TR fluorescence lifetime. Fluorescence lifetime is presented under a Z-score form (*Methods*) and the modulus is normalized to the cell radius setting cell border at R = 1. In *D* and *E*, 15 cells analyzed in one independent experiment. (*F*) Coupling between exocytosis probability and membrane tension using data from *C* and *E*. The estimation of exocytosis probability at a given modulus R is based on the number of events normalized by the corresponding surface, contrarily to *C*. The color code corresponds to the normalized modulus R. Each point is associated to SEM for both axes.

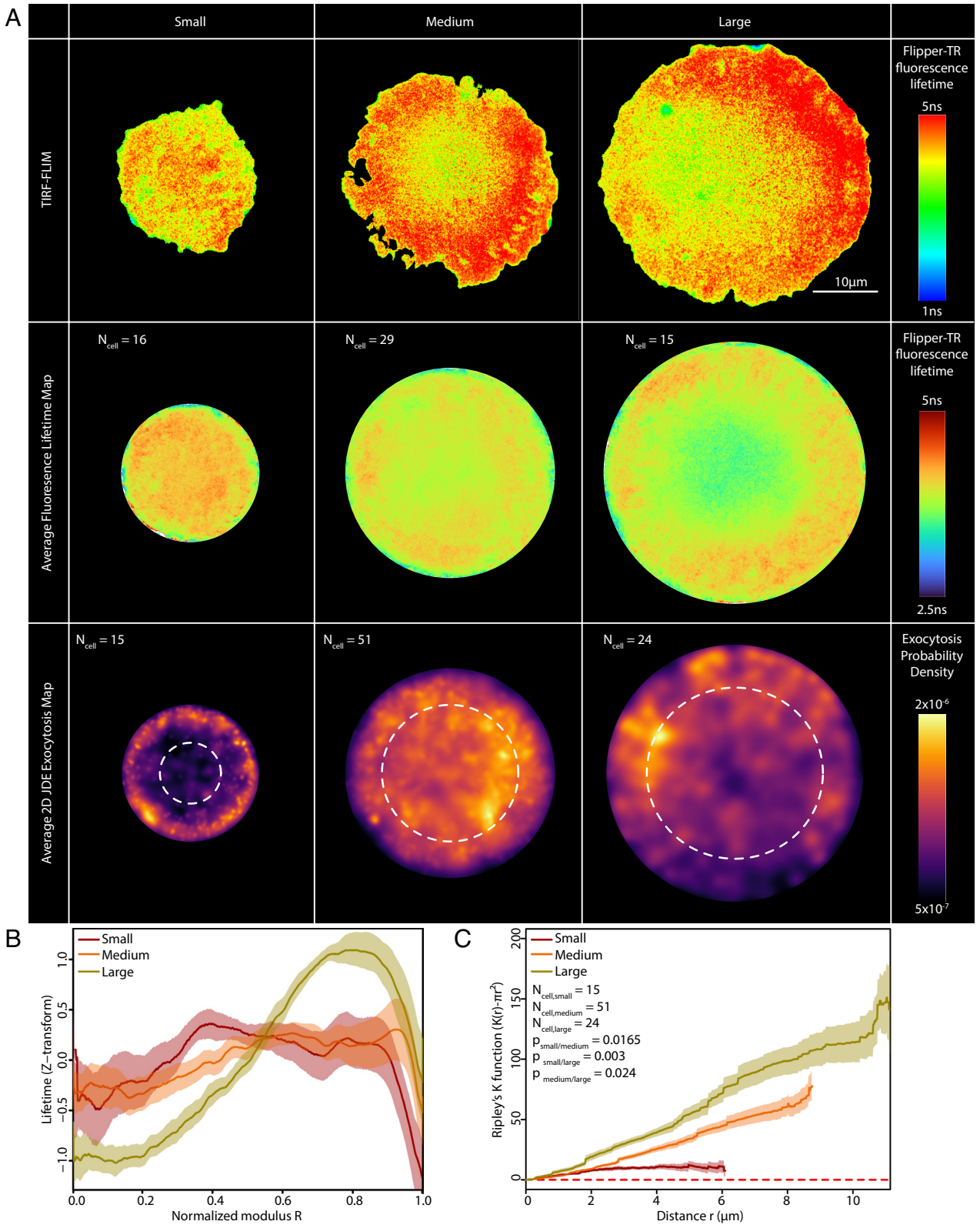

Fig. 5. Strength of Membrane Tension Gradient Correlates with Clustering of Lysosomal Exocytosis. (*A*) Representative images of cells seeded on ring-shaped micropattern of different diameters (classified as small ~25 µm, medium ~35 µm and large ~45 µm) and incubated with Flipper-TR visualized by TIRF-FLIM (*Upper*). The color code represents the Flipper-TR fluorescence lifetime. Average fluorescence lifetime maps for cells seeded on different diameters (*Middle*), maps are an average of FLIM images from n = 16 (small), n = 29 (medium) and n = 15 (large) cells from four independent experiments. Color code represents Flipper-TR fluorescence lifetime. Average exocytosis maps (*Lower*) from n = 15 (small), n = 51 (medium) and n = 24 (large) cells from 11 independent experiments. The color code represents the probability of exocytosis. (*B*) Radial averages ± SEM of the Flipper-TR fluorescence lifetime (data from *A*). Lifetime is presented under a Z-score form (*Methods*) and the modulus is normalized by the cell radius setting cell border at R = 1 for the three conditions. (*C*) Average spatial Ripley's K functions ± SEM of exocytosis in cells seeded on ring-shaped micropatterns with different diameters, small in dark red, medium in orange and large in yellow (data from *A*). The significance of the differences between Ripley's K functions has been evaluated using a permutation test (*Methods*) and *P*-values were corrected using Benjamini–Hochberg procedure. The red-dashed line represents expected curve under CSR hypothesis.

on the spatial organization of membrane tension, which is regulated by the presence and localization of FAs.

Materials and Methods

Cell Culture. hTERT-immortalized retinal pigment epithelial cell line (hTERT RPE-1) were cultivated in DMEM/F12 media (Gibco, catalog # 21041-025) complemented with 10% Fetal Bovine Serum (Eurobio, catalog # CVFSVF00-01) (without antibiotics). Cells were maintained at 37 °C with 5% CO2 in a humidified incubator.

Transfection. Cells were transfected with the following constructs: VAMP7-pHluorin (77), mCh-Rab6A, and Paxillin-mCh (52). Cells are transfected with 800 ng of DNA (or 2 × 400 ng for co-transfection) using the JetPrime kit (Polyplus). Cells were imaged 24 h after transfection.

Drug Treatments. Cells were treated with the following drugs with the given concentration and incubation time: Golgicide A 10 μM 30 min (Merck, catalog # G0923), Bafilomycin A1 100 nM 1 h (MedChemExpress, catalog # HY-100558), Histamine 100 μM cells immediately imaged (Merck, catalog # H7125), PF-573228 10 μM 15 min (Merck, catalog # PZ0117), Nocodazole 10 μM 1 h (Merck, catalog # M1404), Cytochalasin D 500 nM 1 h (Merck, catalog # C8273), Para-nitroblebbistatin 20 μM 15 min (Cayman Chemical Company, item 24171), β-methyl-cyclodextrin 5 mM 15 min (Merck, catalog # C4555). Hypo-osmotic shocks were made by adding water in the media with a volume ratio of 1:1 and cells were imaged 15 min after. For all drug conditions, a paired design has been used: the same cell is imaged before and after the treatment.

Micropatterning. We followed the photolithography micropatterning protocol from Azioune et al. (78). Briefly, coverslips (1.5H ThorLabs, Catalog # CG15XH1) were oxidized by plasma-cleaner (Harrick Plasma) during 5 min. Coverslips were PEG-coated by incubating them on a drop of PLL-g-PEG [Surface Solutions, PLL(20)-g[3.5]- PEG(2)] (0.1 mg/mL diluted in water, 10 mM HEPES, pH = 7.4) in a moiety chamber during 1 h. After coating, patterns were printed using a deep UV lamp (Jelight Company Inc, catalog # 342-220) with radiation passing through a photomask (DeltaMask) during 5 min. Finally, patterns were fibronectin-coated by incubating coverslips on a drop of fibronectin (Merck/Sigma, catalog # F1141) (50 μg/mL diluted in water) and fibrinogen-Alexa647 (Molecular Probes, Invitrogen, catalog # F35200) (or fibrinogen-Alexa488) (5 μg/mL) in a moiety chamber during 1 h. Coverslips were conserved at 4 °C in PBS.

Cell seeding on micropatterns was described in Lachuer et al. (49). Briefly, coverslips were maintained in magnetic chamlides for live imaging or kept in a P6 wells for fixation. ~200,000 trypsinized (Thermo Fisher, catalog # 12605010) cells were added in the chamlide chamber. After 10 min incubation in 37 °C incubator, cells were attached to the substrate. Cells were washed using DMEM/F12 media with 20 mM HEPES (Gibco, catalog # 15630-056) [+2% penicillin/streptomycin (Gibco, catalog # 15140-122] if cells were used for lived-imaging). Cells were incubated at least 3 h in the incubator until full spreading on the micropattern. Cells were imaged the same day.

Different geometries of micropatterns were used. In Fig. 4 and *SI Appendix* Fig. S2, ring-shaped micropatterns with a diameter of 37 μm were employed. In Fig. 5, three sizes of ring-shaped micropatterns were used, with diameters of 25 μm, 35 μm, and 45 μm. For all sizes, the thickness of the adhesive ring was 7 μm. Fig. 5 also includes data of Fig. 4. Despite these theoretical sizes, a variation in the measured cell diameter was observed likely due to UV diffraction during the printing. The actual dimensions were systematically measured. During analysis, cells with diameter inferior to 20 μm were categorized as "Small," between 20 μm and 38 μm as "Medium" and superior to 38 μm as "Large." In *SI Appendix*, Fig. S1, rectangular micropattern has dimensions of 9 × 40 μm.

Microscopy.

TIRFM. Non-patterned cells were seeded in fluorodishes (World Precision Instrument) coated with fibronectin [or PLL (Merck P4707)]. DMEM/F12 media + 20 mM HEPES was used for imaging. Patterned cells were prepared as described. The acquisition was made using an inverted Nikon TIRFM equipped with an EMCCD camera (efficiency 95%) with a 100× objective (pixel size = 0.160 μm). The following lasers were used 491 nm, 561 nm, and 642 nm. Time-lapse of VAMP7-pHluorin was acquired with a frame rate of one image every 300 ms during 5 min. Frame rate was set according to the half-life of exocytosis events. Due to microscopic device delay, the actual frame rate was computed using the computer time of saved files.

TIRF-FLIM. Images were acquired on a homemade setup based on a ×100 1.49 Nikon Objective (79, 80). A 2 MHz supercontinuum laser source (SC450 HE-PP Fianium) was filtered (Excitation filter 482-18, Dichroic Di01-R488, Emission filter Long Pass 488, Semrock) within the microscope cube to match the dye excitation/emission spectra. The average power in the back focal place of the objective was between 30 and 100 μW depending on the experiment. The TIRF angle was finely controlled thanks to a motorized stage which allows one to adjust the pulsed beam focalization in the back focal plane of the TIRFM objective. Fluorescence images were detected thanks to a time-resolved detection based on the use of a high-rate imager (Kentech Ltd., UK) optically relayed to a charge-coupled device camera (ORCA AG, Hamamatsu, binning 2 × 2). This intensifier was synchronized with the laser pulse through a programmable delay line (Kentech, precision programmable 50 Ω delay line), which enables us to open temporal gates with 1 ns width at different times after the pulse, thus sampling the fluorescence decay. Each time gated image corresponds to an average of 10 images (10 × 250 ms). FLIM maps were thus produced by recording a series of 17 time-gated fluorescence intensity images and fitting the data for each image pixel to a single exponential decay model by use of a standard nonlinear least-squares fitting algorithm.

Flipper-TR. Cells were prepared as for classical TIRFM. Fifteen minutes before acquisition, Flipper-TR was added in the media (Spirochrome, Catalog # SC020) (71) at a concentration of 1 μM. If used, drugs were added with Flipper-TR. Cells were not washed as recommended. Due to the high variability of the fluorescence lifetime, a z-score transformation was applied when specified. For each cell, the average μ and SD σ of the fluorescence lifetime was computed. Then, each lifetime pixel x_i value was reduced and centered:

$$z_i = \frac{x_i - \mu}{\sigma}.$$

Immunofluorescence. Cells were fixed with 4% PFA (Euromedex, catalog # 15710) during 15 min and quenched with a 50 mM NH4Cl solution. After PBS washing, cells were permeabilized (and blocked) with a PBS Saponin (MP Biomedicals, catalog # 102855) (0.5 g/L) BSA (Merck, catalog # 10735094001) (1 g/L). Coverslips were incubated during 1 h in a moiety chamber at RT with primary antibodies diluted in a PBS 2% BSA solution. After PBS washing, coverslips were incubated with a secondary antibody (400×) conjugated with a fluorophore following the same protocol. Finally, coverslips were mounted with Mowiol (Biovaley, catalog # MWL4-88-25) and DAPI (Merck, catalog # D8417). The following primary antibodies were used: Syntaxin 3 (100×) (Merck/Sigma, catalog # S5547), Syntaxin 4 (1,000×) (BD Transduction Laboratories, Material # 610439), LAMP1 (100×) (BD Biosciences, catalog # 555798) and Rab11 (100×) (Invitrogen, Ref 700184). The following secondary antibodies were used: Mouse A488 (Interchim 715-545-151), Rabbit A488 (Interchim, 711-545-152), Mouse Cy3 (Interchim, 715-165-151) and Rabbit Cy3 (Interchim, 711-165-152). LysoTracker Deep Red (Invitrogen, Ref L12492) has been used at the concentration of 200 nM and incubated 1 h at 37 °C with cells before fixation.

STX3/4 IF samples were imaged using an inverted videomicroscope with deconvolution (Delta Vision – Applied Precision) equipped with Xenon lamp. Acquisition was made at 100× (pixel size = 65 nm). Images acquired were deconvolved using Softworx (enhanced ratio method).

Rab11/LAMP1/LysoTracker IF samples were imaged using a 3D Deconvolution microscope (Leica DMI-5000B) equipped with a CoolSNAP HQ2 camera. Acquisition was made at 100× (pixel size = 64 nm). Colocalization was been quantified using JACoP imageJ pluggin (81): Manders thresholds have been manually set for each image previously treated with a background subtraction.

Statistical Analysis. All statistical analyses were made with R [R Core Team (2021)] with the help of the following packages: spatsat (50), raster, viridis, ggplot2, dunn.test, ape (82), imager, pracma, circular, ggpur, evmix (83), splancs, OpenImageR, minpack.lm.

Hypothesis testing. The number of cells and the number of independent repetition is indicated in the legend. Since our cells are mostly isolated when imaged, we performed only single cells analysis, each cell is considered as

independent, setting the sample size. The statistical test used is indicated in the legend. Tests are always conducted in a two-sided manner and a multiple comparison correction is applied when needed. We mainly used nonparametric test (Wilcoxon test, Kruskal–Wallis test), and a parametric test (Student *t* test) only when the sample size was high (n > 30). Paired tests were used for all experiments where the same cell is imaged before and after treatment. Finally, correlation was measured by Pearson correlation coefficient and tested with a *t* test.

Intensity Map. The intensity function λ is defined by:

$$E\left[x \in S\right] = \int_S \lambda(u)\, du.$$

With x a pattern of points, u coordinates, S a region of the observation window, and E[x∈n] the expected number of points in S. The intensity map was computed using spatstat function density() with Jones-Diggle improved edge correction. The intensity map can be interpreted and normalized as a density map by dividing it by the total number of points.

Monte Carlo CSR simulations. Monte Carlo simulations were used for two purposes: i) normalization and ii) generation of CSR 95% envelopes.

i) Several measures used depend on the cell geometry and the number of exocytosis events. Therefore, we normalized observed values by CSR simulated values. For each cell, a high number (n = 100) of Monte Carlo simulations was run to generate CSR exocytosis maps associated with the same number of exocytosis events and the same cell geometry. The ratio between observed and average simulated values allows classifying cells in two categories: more extreme or less extreme than CSR compared to the observed measure.

ii) Monte Carlo simulations were used to generate CSR envelopes. Some measures (mainly Ripley's K function) were averaged over a population of cells; therefore CSR simulations were run in the same way: Monte Carlo CSR simulations were run for the full population of cells and the evaluated quantity is averaged over the different simulated cells. This procedure was repeated a high number of times (n = 100). The CSR envelope contains 95% of these simulations.

NND. The NND of a given exocytosis event is the distance to the closest exocytosis event. These distances give information on the short scale spatial structure. NND was used to test CSR hypothesis according to the procedure presented in Lachuer et al. (49) and detailed in the Monte Carlo section. Simulated average NND are compared to the observed NND. This allowed to classify the cell as clustered ($NND_{observed} < NND_{simulated}$), or dispersed ($NND_{observed} > NND_{simulated}$). Note that temporal NND were treated similarly to spatial NND, just by reducing the dimension of the analysis.

Ripley's K function. For a point pattern $X = \{x_1, x_2, \ldots, x_n\}$ where each x is point coordinates observed in an area $|\Omega|$, the Ripley's K function (84, 85) is defined as:

$$K(r) = \frac{|\Omega|}{n(n-1)} \sum_{i=1}^{n} \sum_{j \neq i} 1_{|x_i - x_j| \leq r}.$$

This function quantifies the average number of points in a disk of radius r centered on one point. In case of CSR, this function should be close to πr^2. Therefore we always substrate πr^2 to K(r), a positive value indicates clustering whereas a negative value indicates dispersing. The spatial Ripley's K function was computed using spatstat function Kest() with the best edge correction possible. Ripley's K function was computed between 0 and a quarter of the cell size to avoid edge effects. All Ripley's K functions plotted are an average of a population of Ripley's K functions (±SEM). A permutation test (with 999 permutations) based on a Studentized distance is used to compare populations thanks to the sptatstat function studpermu.test() (86). Finally, a CSR 95% envelope was computed with Monte-Carlo simulations (see corresponding section).

Temporal Ripley's K function K(t) is the reduction of the 2D spatial Ripley's K function in 1D. Therefore the expected value under CSR hypothesis is 2t. K(t) was computed by our own function using the Ripley's edge correction following (87). Temporal Ripley's K function was treated in the same way as the spatial one to generate the CSR 95% envelope and for the averaging.

Spatiotemporal Ripley's K function K(r,t) is the 3D extension of the spatial Ripley's K function that evaluates the number of neighbors in a cylinder of a radius r and a half height t (88). K(r,t) was computed using the splancs function stkhat(). The median K(r,t) was computed (averaging is avoided due to the generation of aberrant values by splancs). In absence of spatiotemporal coupling (i.e., independency of the temporal and spatial point coordinates):

$$D = K(r,t) - K(r)\,K(t) = 0.$$

Thereby the independency can be evaluated by the D statistics. It can be statistically tested using a permutation test (1,000 permutations) using the splancs function stmctest().

Distance to cell border. Distance to cell border was computed using imager function distance_transform(). For each cell, the distance to cell border at exocytosis sites was measured.

The significance at the single cell level was accessed using Monte Carlo simulations (see corresponding section). Observed cell border distances were divided by the average simulated cell border distances allowing a classification of the cells into two categories: borders-avoiding (ratio > 1) or borders-prefering (ratio < 1).

Anisotropy. The cell was cut in 30 angular sections (from the center of mass). An angle Θ_i was associated to each section. The number of exocytosis event was computed in each section and divided by the surface of the corresponding section giving a coefficient w_i (normalized by the sum of the coefficients). The anisotropy/polarization measurement is based on the average resultant length computed as:

$$R = \sqrt{\left(\sum_{i=1}^{30} w_i cos\left(\theta_i\right)\right)^2 + \left(\sum_{i=1}^{30} w_i sin\left(\theta_i\right)\right)^2}.$$

This polarization index ranged between 0 and 1. The significance was accessed using Monte Carlo simulations (see corresponding section). Observed average resultant lengths were divided by the average simulated resultant length allowing a classification of the cells into two categories: polarized (ratio > 1) or non-polarized (ratio < 1).

Exocytosis-FA co-appearing index. The average paxillin fluorescence intensity was measured at the locations of exocytosis event. The significance was accessed using Monte Carlo simulations (see corresponding section). The comparison of the observed average intensity with simulated ones allows classifying cells with a colocalization index (I_{obs}/I_{sim}) under two categories: co-appearing ($I_{obs}/I_{sim} > 1$), no-co-appearing ($I_{obs}/I_{sim} < 1$). The separation of central and peripheral FAs subpopulations in S2D has been done according to a threshold distance from cell borders. FAs with a distance superior to 3 μm from cell borders are classified as central, whereas the others are classified as peripheral. Note that we tested different threshold distances and the analysis remained robust and leads to similar conclusions.

Modulus distribution. On micropatterns, exocytosis events were described with polar coordinates (with the origin at the center of the pattern). The modulus is the distance between an event and the center (normalized by the cell radius). For each cell a modulus distribution was computed using KDE. To avoid boundary effects, an asymmetric beta kernel was used (89) using the evmix function dbckden(). The depicted modulus distribution is an average over the population ±SEM. This distribution can be compared to the expected distribution in case of CSR:

$$p_{CSR}(r) = 2r.$$

The 95% CSR envelope was computed using Monte-Carlo simulations (see corresponding section). Despite beta edge correction, the simulations do not fit perfectly p_{csr}. In order to avoid any bias due to kernels, we also conducted the same analysis using empirical cumulative distributions. The empirical cumulative distribution P_{CSR} under CSR hypothesis is:

$$P_{CSR}(r) = \int_0^r p_{CSR}(x)\, dx = r^2.$$

Fourier analysis. Fourier analysis was conducted using fast Fourier transform function fft(). The spectrum of modulus was computed for each cell between 0 and Nyquist frequency. Modulus spectrum were averaged over the cell population.

Moran's I. Moran's I evaluates the spatial auto-correlation (90). We used it to evaluate the spatial structure of lifetime measurement. For an image of N pixels, the Moran's I is defined as:

$$I = \frac{N}{\sum_{i=1}^{N}\sum_{j=1}^{N} w_{i,j}} \frac{\sum_{i=1}^{N}\sum_{j=1}^{N} w_{i,j}\left(x_i-\bar{x}\right)\left(x_j-\bar{x}\right)}{\sum_{i=1}^{N}\left(x_i-\bar{x}\right)^2}.$$

With x_i the i^{th} pixel value, $\bar{x}$ the average pixel values, and w_{ij} the inverse of the Euclidian distance between pixel i and j. This index is superior to -1/(N-1) in case of pixel clustering and inferior to in case of regular spacing (*i.e.,* pixels with similar values are regularly separated). A decreased of the Moran's I should be perceived as a spatial decorrelation *i.e.* pixels are less clustered. Moran's I index was computed using ape function Moran.I() using a random subsample of pixels (Monte Carlo random sampling scheme) to keep a decent computation time.

Image Analysis.

Exocytosis detection. Exocytosis events were detected manually (because automatization failed to reach our exigency level). However some events were probably missed (false negative). This is not a problem, because Ripley's K function is invariant under random thinning (50). It is also likely that some events did not correspond to exocytosis (false positive). Due to the superposition principle (50), the experimental Ripley's K function is the sum of the exocytosis Ripley's K function and the one of false annotation. Therefore, under the assumption that these false annotations are random, possible false annotations could only slightly underestimates clustering.

Half-life. Fluorescence intensity was measured at exocytosis event localizations in a window of 1.12 µm centered on the event through time. The intensity was divided by the intensity at the beginning of the event normalizing the exocytosis peak at one. The intensity profile of all events in a cell was averaged. The intensity was fitted on this averaged profile over 20 frames (~8 s) with a single exponential function:

$$I(t) = Ae^{-t/t_{1/2}} + B.$$

With $t_{1/2}$ the half-life. The fitting was performed with the minpack.lm function nlsLM(). The profile depicted is the average over multiple cells. The half-life obtained from this average curve is close to the lifetime averaged over multiple cells.

Segmentation. Cell segmentation to obtain mask or segmentation of syntaxin patches was performed using manual thresholding with ImageJ software.

Data, Materials, and Software Availability. All data relevant to the article have been deposited in Github (91). Other study data are included in the article and/or *SI Appendix*.

ACKNOWLEDGMENTS. We are grateful to Sabine Bardin, Pallavi Mathur, David Pereira, Tarn Duong, Mathieu Coppey and Pierre Sens for fruitful discussions and/or help at the bench. We also thank Mathieu Piel lab for sharing photomasks, Thierry Galli for the VAMP7-pHluorin plasmid and syntaxin antibodies, and Marc Tramier and Giulia Bertolin for testing Flipper-TR with their FAST-FLIM. Finally, we thank (again) Thierry Galli and Christophe Lamaze for critical reading of the manuscript. We greatly acknowledge the Nikon Imaging Centre @ Institut Curie-CNRS, member of the French National Research Infrastructure France-BioImaging (ANR10-INSB-04). This work was supported by ARC (Association pour la Recherche sur le Cancer) PhD fellowship, FRM (Fondation Recherche Médicale) PhD extension fellowship, the ITMO Nanotumor grant to KS and grants from the Labex Cell(n)Scale (11-LBX-0038) and the Idex Paris Sciences et Lettres (ANR-10-IDEX-0001-02 PSL).

Author affiliations: [a]Institut Curie, Paris Sciences et Lettres Research University, CNRS UMR 144 Cell Biology and Cancer, 75005 Paris, France; [b]Université Paris-Saclay, CNRS, Institut des Sciences Moléculaires d'Orsay 91405, Orsay, France; and [c]Tumor Cell Dynamics Unit, Inserm U1279 Gustave Roussy Institute, Université Paris-Saclay, Villejuif 94800, France

1. T. H. Kloepper, C. N. Kienle, D. Fasshauer, An elaborate classification of SNARE proteins sheds light on the conservation of the eukaryotic endomembrane system. *Mol. Biol. Cell* **18**, 3463–3471 (2007), 10.1091/mbc.E07-03-0193.
2. E. Neveu, D. Khalifeh, N. Salamin, D. Fasshauer, Prototypic SNARE roteins are encoded in the genomes of heimdallarchaeota, potentially bridging the gap between the prokaryotes and eukaryotes. *Curr. Biol.* **30**, 2468–2480.e5 (2020), 10.1016/j.cub.2020.04.060.
3. M. A. Samie, H. Xu, Lysosomal exocytosis and lipid storage disorders. *J. Lipid Res.* **55**, 995–1009 (2014), 10.1194/jlr.R046896.
4. J. Kowal, M. Tkach, C. Théry, Biogenesis and secretion of exosomes. *Curr. Opin. Cell Biol.* **29**, 116–125 (2014), 10.1016/j.ceb.2014.05.004.
5. N. W. Andrews, M. Corrotte, Plasma membrane repair. *Curr. Biol.* **28**, R392–R397 (2020), 10.1016/j.cub.2017.12.034.
6. R. M. E. Arantes, N. W. Andrews, A role for synaptotagmin VII-regulated exocytosis of lysosomes in neurite outgrowth from primary sympathetic neurons. *J. Neurosci.* **26**, 4630–4637 (2006), 10.1523/JNEUROSCI.0009-06.2006.
7. G. Chen *et al.*, Lysosomal exocytosis in Schwann cells contributes to axon remyelination. *Glia* **60**, 295–305 (2012), 10.1002/glia.21263.
8. Y. Dou *et al.*, Microglial migration mediated by ATP-induced ATP release from lysosomes. *Cell Res.* **22**, 1022–1033 (2012), 10.1038/cr.2012.10.
9. K. K. Huynh, J. G. Kay, J. L. Stow, S. Grinstein, Fusion, fission, and secretion during phagocytosis. *Physiology* **22**, 366–372 (2007), 10.1152/physiol.00028.2007.
10. P. J. Peters *et al.*, Cytotoxic T lymphocyte granules are secretory lysosomes, containing both perforin and granzymes. *J. Exp. Med.* **173**, 1099–1109 (1991), 10.1084/jem.173.5.1099.
11. H. J. Geuze, The role of endosomes and lysosomes in MHC class II functioning. *Immunol. Today* **19**, 282–287 (1998), 10.1016/S0167-5699(98)01269-9.
12. J. Lacombe, G. Karsenty, M. Ferron, Regulation of lysosome biogenesis and functions in osteoclasts. *Cell Cycle Georget. Tex* **12**, 2744–2752 (2013), 10.4161/cc.25825.
13. S. Ghosh *et al.*, β-coronaviruses use lysosomes for egress instead of the biosynthetic secretory pathway. *Cell* **183**, 1520–1535.e14 (2020), 10.1016/j.cell.2020.10.039.
14. D. Chen *et al.*, ORF3a of SARS-CoV-2 promotes lysosomal exocytosis-mediated viral egress. *Dev. Cell* **56**, 3250–3263.e5 (2021), 10.1016/j.devcel.2021.10.006.
15. D. Hoshino *et al.*, Exosome secretion is enhanced by invadopodia and drives invasive behavior. *Cell Rep.* **5**, 1159–1168 (2013), 10.1016/j.celrep.2013.10.050.
16. E. Machado *et al.*, Regulated lysosomal exocytosis mediates cancer progression. *Sci. Adv.* **1**, e1500603 (2015), 10.1126/sciadv.1500603.
17. J. M. LaPlante *et al.*, Lysosomal exocytosis is impaired in mucolipidosis type IV. *Mol. Genet. Metab.* **89**, 339–348 (2006), 10.1016/j.ymgme.2006.05.016.
18. P. Novick, C. Field, R. Schekman, Identification of 23 complementation groups required for post-translational events in the yeast secretory pathway. *Cell* **21**, 205–215 (1980), 10.1016/0092-8674(80)90128-2.
19. T. Söllner *et al.*, SNAP receptors implicated in vesicle targeting and fusion. *Nature* **362**, 318–324 (1993), 10.1038/362318a0.
20. R. Fernández-Chacón *et al.*, Synaptotagmin I functions as a calcium regulator of release probability. *Nature* **410**, 41–49 (2001), 10.1038/35065004.
21. E. D. Gundelfinger, M. M. Kessels, B. Qualmann, Temporal and spatial coordination of exocytosis and endocytosis. *Nat. Rev. Mol. Cell Biol.* **4**, 127–139 (2003), 10.1038/nrm1016.
22. H. Kasai, N. Takahashi, H. Tokumaru, Distinct initial SNARE configurations underlying the diversity of exocytosis. *Physiol. Rev.* **92**, 1915–1964 (2012), 10.1152/physrev.00007.2012.
23. T. C. Südhof, The presynaptic active zone. *Neuron* **75**, 11–25 (2012), 10.1016/j.neuron.2012.06.012.
24. J. Schmoranzer, M. Goulian, D. Axelrod, S. M. Simon, Imaging constitutive exocytosis with total internal reflection fluorescence microscopy. *J. Cell Biol.* **149**, 23–32 (2000).
25. P. Keller, D. Toomre, E. Díaz, J. White, K. Simons, Multicolour imaging of post-Golgi sorting and trafficking in live cells. *Nat. Cell Biol.* **3**, 140–149 (2001), 10.1038/35055042.
26. R. Sebastian *et al.*, Spatio-temporal analysis of constitutive exocytosis in epithelial cells. *IEEE/ACM Trans. Comput. Biol. Bioinform.* **3**, 17–32 (2006), 10.1109/TCBB.2006.11.
27. T. Yuan, J. Lu, J. Zhang, Y. Zhang, L. Chen, Spatiotemporal detection and analysis of exocytosis reveal fusion "hotspots" organized by the cytoskeleton in endocrine cells. *Biophys. J.* **108**, 251–260 (2015), 10.1016/j.bpj.2014.11.3462.
28. F. L. Urbina, S. M. Gomez, S. L. Gupton, Spatiotemporal organization of exocytosis emerges during neuronal shape change. *J. Cell Biol.* **217**, 1113–1128 (2020), 10.1083/jcb.201709064.
29. J. Fu *et al.*, A glucose-dependent spatial patterning of exocytosis in human β-cells is disrupted in type 2 diabetes. *JCI Insight* **5**, 127896 (2019), 10.1172/jci.insight.127896.
30. K. Schauer *et al.*, Probabilistic density maps to study global endomembrane organization. *Nat. Methods* **7**, 560–566 (2010), 10.1038/nmeth.1462.
31. Q. Ba, G. Raghavan, K. Kiselyov, G. Yang, Whole-cell scale dynamic organization of lysosomes revealed by spatial statistical analysis. *Cell Rep.* **23**, 3591–3606 (2020), 10.1016/j.celrep.2018.05.079.
32. J. Xu *et al.*, Mechanism of polarized lysosome exocytosis in epithelial cells. *J. Cell Sci.* **125**, 5937–5943 (2012), 10.1242/jcs.109421.
33. S. Martinez-Arca, P. Alberts, A. Zahraoui, D. Louvard, T. Galli, Role of tetanus neurotoxin insensitive vesicle-associated membrane protein (TI-VAMP) in vesicular transport mediating neurite outgrowth. *J. Cell Biol.* **149**, 889–900 (2000), 10.1083/jcb.149.4.889.
34. V. Proux-Gillardeaux, G. Raposo, T. Irinopoulou, T. Galli, Expression of the Longin domain of TI-VAMP impairs lysosomal secretion and epithelial cell migration. *Biol. Cell* **99**, 261–271 (2007), 10.1042/BC20060097.
35. C. Verderio *et al.*, TI-VAMP/VAMP7 is the SNARE of secretory lysosomes contributing to ATP secretion from astrocytes. *Biol. Cell* **104**, 213–228 (2012), 10.1111/boc.201100070.
36. T. Galli *et al.*, A novel tetanus neurotoxin-insensitive vesicle-associated membrane protein in SNARE complexes of the apical plasma membrane of epithelial cells. *Mol. Biol. Cell* **9**, 1437–1448 (1998), 10.1091/mbc.9.6.1437.

37. G. F. Vogel *et al.*, Cargo-selective apical exocytosis in epithelial cells is conducted by Myo5B, Slp4a, Vamp7, and Syntaxin 3. *J. Cell Biol.* **211**, 587–604 (2015), 10.1083/jcb.201506112.
38. K. C. Williams, R. E. McNeilly, M. G. Coppolino, SNAP23, Syntaxin4, and vesicle-associated membrane protein 7 (VAMP7) mediate trafficking of membrane type 1-matrix metalloproteinase (MT1-MMP) during invadopodium formation and tumor cell invasion. *Mol. Biol. Cell* **25**, 2061–2070 (2014), 10.1091/mbc.E13-10-0582.
39. D. M. Ward, J. Pevsner, M. A. Scullion, M. Vaughn, J. Kaplan, Syntaxin 7 and VAMP-7 are soluble N-ethylmaleimide-sensitive factor attachment protein receptors required for late endosome-lysosome and homotypic lysosome fusion in alveolar macrophages. *Mol. Biol. Cell* **11**, 2327–2333 (2000), 10.1091/mbc.11.7.2327.
40. N. Wade *et al.*, Syntaxin 7 complexes with mouse Vps10p Tail interactor 1b, syntaxin 6, vesicle-associated membrane protein (VAMP)8, and VAMP7 in B16 melanoma cells*. *J. Biol. Chem.* **276**, 19820–19827 (2001), 10.1074/jbc.M010838200.
41. A. Bogdanovic *et al.*, Syntaxin 7, syntaxin 8, Vti1 and VAMP7 (vesicle-associated membrane protein 7) form an active SNARE complex for early macropinocytic compartment fusion in Dictyostelium discoideum. *Biochem. J.* **368**, 29–39 (2002), 10.1042/BJ20020845.
42. R. Ikarashi *et al.*, Regulation of molecular clock oscillations and phagocytic activity via muscarinic Ca2+ signaling in human retinal pigment epithelial cells. *Sci. Rep.* **7**, 44175 (2017), 10.1038/srep44175.
43. W. Kwon, S. A. Freeman, Phagocytosis by the retinal pigment epithelium: Recognition, resolution, Recycling. *Front. Immunol.* **11**, 604205 (2020).
44. M. Chaineau, L. Danglot, T. Galli, Multiple roles of the vesicular-SNARE TI-VAMP in post-Golgi and endosomal trafficking. *FEBS Lett.* **583**, 3817–3826 (2009), 10.1016/j.febslet.2009.10.026.
45. A. Burgo *et al.*, A molecular network for the transport of the TI-VAMP/VAMP7 vesicles from cell center to periphery. *Dev. Cell* **23**, 166–180 (2012), 10.1016/j.devcel.2012.04.019.
46. J. B. Saenz *et al.*, Golgicide A reveals essential roles for GBF1 in Golgi assembly and function. *Nat. Chem. Biol.* **5**, 157–165 (2009), 10.1038/nchembio.144.
47. F. J. Verweij *et al.*, Quantifying exosome secretion from single cells reveals a modulatory role for GPCR signaling. *J. Cell Biol.* **217**, 1129–1142 (2020), 10.1083/jcb.201703206.
48. P. Diggle, *Statistical Analysis of Spatial Point Patterns* (Academic Press, 1983).
49. H. Lachuer, P. Mathur, K. Bleakley, K. Schauer, Quantifying spatiotemporal parameters of cellular exocytosis in micropatterned cells. *J. Vis. Exp.* **16**, 163 (2020), 10.3791/60801.
50. A. Baddeley, E. Rubak, R. Turner, *Spatial Point Patterns: Methodology and Applications with R* (Chapman and Hall/CRC, 2015).
51. N. Schiefermeier *et al.*, The late endosomal p14-MP1 (LAMTOR2/3) complex regulates focal adhesion dynamics during cell migration. *J. Cell Biol.* **205**, 525–540 (2014), 10.1083/jcb.201310043.
52. L. Fourriere *et al.*, RAB6 and microtubules restrict protein secretion to focal adhesions. *J. Cell Biol.* **218**, 2215–2231 (2019), 10.1083/jcb.201805002.
53. S. K. Mitra, D. A. Hanson, D. D. Schlaepfer, Focal adhesion kinase: In command and control of cell motility. *Nat. Rev. Mol. Cell Biol.* **6**, 56–68 (2005), 10.1038/nrm1549.
54. J. K. Slack-Davis *et al.*, Cellular characterization of a novel focal adhesion kinase inhibitor *. *J. Biol. Chem.* **282**, 14845–14852 (2007), 10.1074/jbc.M606695200.
55. S. Stehbens, T. Wittmann, Targeting and transport: How microtubules control focal adhesion dynamics. *J. Cell Biol.* **198**, 481–489 (2012), 10.1083/jcb.201206050.
56. S. J. Stehbens *et al.*, CLASPs link focal-adhesion-associated microtubule capture to localized exocytosis and adhesion site turnover. *Nat. Cell Biol.* **16**, 561–573 (2014), 10.1038/ncb2975.
57. S. Seetharaman, S. Etienne-Manneville, Microtubules at focal adhesions – a double-edged sword. *J. Cell Sci.* **132**, jcs232843 (2019), 10.1242/jcs.232843.
58. P. Miklavc, M. Frick, Actin and myosin in non-neuronal exocytosis. *Cells* **9**, 1455 (2020), 10.3390/cells9061455.
59. N. C. Gauthier, M. A. Fardin, P. Roca-Cusachs, M. P. Sheetz, Temporary increase in plasma membrane tension coordinates the activation of exocytosis and contraction during cell spreading. *Proc. Natl. Acad. Sci. U.S.A.* **108**, 14467–14472 (2011), 10.1073/pnas.1105845108.
60. P. J. Wen *et al.*, Actin dynamics provides membrane tension to merge fusing vesicles into the plasma membrane. *Nat. Commun.* **7**, 12604 (2016), 10.1038/ncomms12604.
61. T.-T. Kliesch *et al.*, Membrane tension increases fusion efficiency of model membranes in the presence of SNAREs. *Sci. Rep.* **7**, 12070 (2017), 10.1038/s41598-017-12348-w.
62. Z. Shi, Z. T. Graber, T. Baumgart, H. A. Stone, A. E. Cohen, Cell membranes resist flow. *Cell* **175**, 1769–1779.e13 (2020), 10.1016/j.cell.2018.09.054.
63. G. Wang, T. Galli, Reciprocal link between cell biomechanics and exocytosis. *Traffic* **19**, 741–749 (2020), 10.1111/tra.12584.
64. G. Wang *et al.*, Biomechanical control of lysosomal secretion via the VAMP7 hub: A tug-of-war between VARP and LRRK1. *iScience* **4**, 127–143 (2020), 10.1016/j.isci.2018.05.016.
65. C. Roffay *et al.*, Passive coupling of membrane tension and cell volume during active response of cells to osmosis. *Proc. Natl. Acad. Sci. U.S.A.* **118**, e2103228118 (2021), 10.1073/pnas.2103228118.
66. M. Zwiewka, T. Nodzyński, S. Robert, S. Vanneste, J. Friml, Osmotic stress modulates the balance between exocytosis and clathrin-mediated endocytosis in Arabidopsis thaliana. *Mol. Plant* **8**, 1175–1187 (2015), 10.1016/j.molp.2015.03.007.
67. F. Mao, Y. Yang, H. Jiang, Endocytosis and exocytosis protect cells against severe membrane tension variations. *Biophys. J.* **120**, 5521–5529 (2021), 10.1016/j.bpj.2021.11.019.
68. B. Hissa, P. W. Oakes, B. Pontes, G. Ramírez-San Juan, M. L. Gardel, Cholesterol depletion impairs contractile machinery in neonatal rat cardiomyocytes. *Sci. Rep.* **7**, 43764 (2017), 10.1038/srep43764.
69. A. Biswas, P. Kashyap, S. Datta, T. Sengupta, B. Sinha, Cholesterol depletion by MβCD enhances cell membrane tension and its variations-reducing integrity. *Biophys. J.* **116**, 1456–1468 (2019), 10.1016/j.bpj.2019.03.016.
70. C. D. Cox, Y. Zhang, Z. Zhou, T. Walz, B. Martinac, Cyclodextrins increase membrane tension and are universal activators of mechanosensitive channels. *Proc. Natl. Acad. Sci. U.S.A.* **118**, e2104820118 (2021), 10.1073/pnas.2104820118.
71. A. Colom *et al.*, A fluorescent membrane tension probe. *Nat. Chem.* **10**, 1118–1125 (2020), 10.1038/s41557-018-0127-3.
72. C. A. Coomer *et al.*, Single-cell glycolytic activity regulates membrane tension and HIV-1 fusion. *PLoS Pathog.* **16**, e1008359 (2020), 10.1371/journal.ppat.1008359.
73. S. L. Gupton, F. B. Gertler, Integrin signaling switches the cytoskeletal and exocytic machinery that drives neuritogenesis. *Dev. Cell* **18**, 725–736 (2010), 10.1016/j.devcel.2010.02.017.
74. A. E. Cohen, Z. Shi, Do cell membranes flow like honey or jiggle like jello? *BioEssays* **42**, 1900142 (2020), 10.1002/bies.201900142.
75. A. D. Lieber, Y. Schweitzer, M. M. Kozlov, K. Keren, Front-to-rear membrane tension gradient in rapidly moving cells. *Biophys. J.* **108**, 1599–1603 (2015), 10.1016/j.bpj.2015.02.007.
76. Y. Schweitzer, A. D. Lieber, K. Keren, M. M. Kozlov, Theoretical analysis of membrane tension in moving cells. *Biophys. J.* **106**, 84–92 (2014), 10.1016/j.bpj.2013.11.009.
77. M. Chaineau, L. Danglot, V. Proux-Gillardeaux, T. Galli, Role of HRB in clathrin-dependent endocytosis. *J. Biol. Chem.* **283**, 34365–34373 (2008), 10.1074/jbc.M804587200.
78. A. Azioune, N. Carpi, Q. Tseng, M. Théry, M. Piel, Protein micropatterns: A direct printing protocol using deep UVs. *Methods Cell Biol.* **97**, 133–146 (2010), 10.1016/S0091-679X(10)97008-8.
79. P. Blandin *et al.*, Time-gated total internal reflection fluorescence microscopy with a supercontinuum excitation source. *Appl. Opt.* **48**, 553–559 (2009), 10.1364/ao.48.000553.
80. C. Marquer *et al.*, Local cholesterol increase triggers amyloid precursor protein-Bace1 clustering in lipid rafts and rapid endocytosis. *FASEB J. Off. Publ. Fed. Am. Soc. Exp. Biol.* **25**, 1295–1305 (2011), 10.1096/fj.10-168633.
81. S. Bolte, F. P. Cordelières, A guided tour into subcellular colocalization analysis in light microscopy. *J. Microsc.* **224**, 213–232 (2006), 10.1111/j.1365-2818.2006.01706.x.
82. E. Paradis, K. Schliep, Ape 5.0: An environment for modern phylogenetics and evolutionary analyses in R. *Bioinformatics* **35**, 526–528 (2019), 10.1093/bioinformatics/bty633.
83. Y. Hu, C. Scarrott, evmix: An r package for extreme value mixture modeling, threshold estimation and boundary corrected kernel density estimation. *J. Stat. Softw.* **84**, 1–27 (2018), 2018.18637/jss.v084.i05.
84. B. D. Ripley, The second-order analysis of stationary point processes. *J. Appl. Probab.* **13**, 255–266 (1976), 10.2307/3212829.
85. P. M. Dixon, "Ripley's K function" in *Wiley StatsRef: Statistics Reference Online* (John Wiley & Sons, Ltd, 2014), 10.1002/9781118445112.stat07751..
86. U. Hahn, A studentized permutation test for the comparison of spatial point patterns. *J. Am. Stat. Assoc.* **107**, 754–764 (2012), 10.1080/01621459.2012.688463.
87. M. L. Yunta, T. Lagache, J. Santi-Rocca, P. Bastin, J.-C. Olivo-Marin, "A statistical analysis of spatial clustering along cell filaments using Ripley's K function" in *2014 IEEE 11th International Symposium on Biomedical Imaging (ISBI)* (2014), pp. 541–544, 10.1109/ISBI.2014.6867928.
88. P. J. Diggle, A. G. Chetwynd, R. Häggkvist, S. E. Morris, Second-order analysis of space-time clustering. *Stat. Methods Med. Res.* **4**, 124–136 (1995), 10.1177/096228029500400203.
89. S. X. Chen, Beta kernel estimators for density functions. *Comput. Stat. Data Anal.* **31**, 131–145 (1999), 10.1016/S0167-9473(99)00010-9.
90. P. A. P. Moran, Notes on continuous stochastic phenomena. *Biometrika* **37**, 17–23 (1950), 10.2307/2332142.
91. H. Lachuer *et al.*, PNAS---Spatial-organization-of-lysosomal-exocytosis-relies-on-membrane-tension-gradients. *Github*. https://github.com/GoudTeam/PNAS---Spatial-organization-of-lysosomal-exocytosis-relies-on-membrane-tension-gradients. Deposited 29 January 2023.